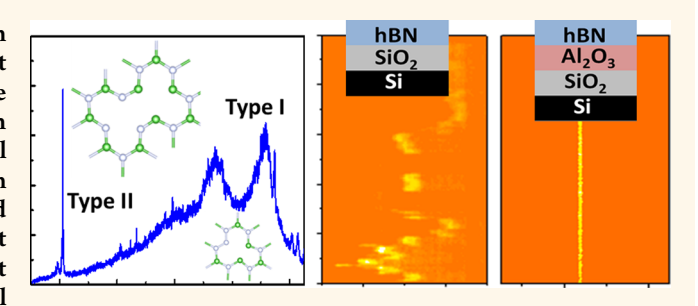


# Nonmagnetic Quantum Emitters in Boron Nitride with Ultranarrow and Sideband-Free **Emission Spectra**

Xiangzhi Li,<sup>†</sup> Gabriella D. Shepard,<sup>†</sup> Andrew Cupo,<sup>†,‡</sup> Nicolas Camporeale,<sup>†</sup> Kamran Shayan,<sup>†</sup> Yue Luo,<sup>†</sup> Vincent Meunier, and Stefan Strauf\*, on

Supporting Information

ABSTRACT: Hexagonal boron nitride (hBN) is an emerging material in nanophotonics and an attractive host for color centers for quantum photonic devices. Here, we show that optical emission from individual quantum emitters in hBN is spatially correlated with structural defects and can display ultranarrow zero-phonon line width down to 45  $\mu$ eV if spectral diffusion is effectively eliminated by proper surface passivation. We demonstrate that undesired emission into phonon sidebands is largely absent for this type of emitter. In addition, magneto-optical



characterization reveals cycling optical transitions with an upper bound for the g-factor of 0.2 ± 0.2. Spin-polarized density functional theory calculations predict possible commensurate transitions between like-spin electron states, which are in excellent agreement with the experimental nonmagnetic defect center emission. Our results constitute a step toward the realization of narrowband quantum light sources and the development of spin-photon interfaces within 2D materials for future chip-scale quantum networks.

**KEYWORDS:** hexagonal boron nitride, spectral diffusion, antibunching, g-factor, 2D materials, color center, density functional theory

exagonal boron nitride (hBN) is a van der Waals material featuring a large band gap (5.95 eV), which makes it attractive as an ultrathin dielectric insulator, for example, in field-effect transistors made from 2D materials such as graphene or transition metal dichalcogenides (TMDCs) as well as a passivation layer in heterostructures made from 2D materials.<sup>2-6</sup> Similar to diamond<sup>7,8</sup> and silicon carbide,<sup>9,10</sup> the hBN crystal lattice can also incorporate color centers, providing electronic states within the band gap. Individual color centers are of particular interest to develop on-chip room temperature quantum light sources<sup>11</sup> as well as spin—photon interfaces.<sup>12</sup> Recent demonstrations in 2D hBN include room temperature single-photon emission in the visible range<sup>13</sup> and electrically driven single-photon emission in the ultraviolet spectral range at cryogenic temperatures.<sup>14</sup> The microscopic origin of quantum emitters that typically emit in the vicinity of 1.9-2.2 eV was predicted by density functional theory (DFT) calculations to be intrinsic and related to a nitrogen vacancy paired with a nitrogen antisite atom (N<sub>B</sub>V<sub>N</sub>).<sup>13</sup> Experimental evidence that the defect center has its origin in native vacancies is found in activation studies that demonstrate color center formation under chemical etching, electron beam irradiation, ion implantation, and thermal gas annealing, 13-19 similar to earlier work on NV center activation in diamond. This defect center is characterized by a rather broad zero-phonon line (ZPL) of several meV as well as dominant optical phonon sidebands (PSB) about 160-170 meV lower in energy. 17,19 The broad line width and strong phonon coupling are rather detrimental properties for quantum optical applications. As a phenomenological characterization, we call this defect the "type I" emitter in the following.

While coupling of color centers to dielectric microcavity resonators could overcome the shortfalls of the type I emitter to some extent,<sup>20</sup> it would be of great interest to investigate alternative color centers in hBN with sufficiently small PSB contribution similar to the diamond platform containing chromium-based color centers with ultranarrow line width<sup>21</sup> or silicon vacancy centers for which coherent population trapping was already demonstrated. <sup>22</sup> To this end, two recent

Received: January 28, 2017 Accepted: May 18, 2017 Published: May 18, 2017

<sup>&</sup>lt;sup>†</sup>Department of Physics & Engineering Physics, Stevens Institute of Technology, Castle Point on Hudson, Hoboken, New Jersey 07030, United States

<sup>&</sup>lt;sup>‡</sup>Department Department of Physics, Applied Physics, and Astronomy, Rensselaer Polytechnic Institute, Troy, New York 12180, United States

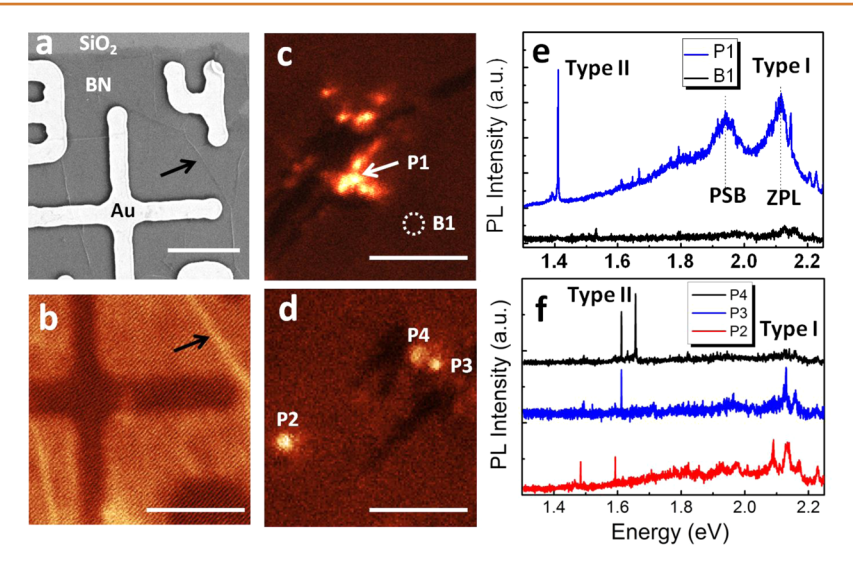


Figure 1. Correlation of optical emission spectra from hBN with spatial and PL imaging. (a) Scanning electron microscope image of multilayer hBN on a  $SiO_2$  substrate with gold marker. (b) PL mapping over the same area recorded with a 550 nm long-pass filter that blocks the 532 nm excitation laser stray light. (c,d) PL mapping in the vicinity of structural defects in the hBN layer. P1–P4 labels locations with particularly bright optical emission, whereas B1 highlights the region from which the background was taken. (e,f) Corresponding optical emission spectra to locations P1–P4 as well as B1 highlighted in (c,d). The energy difference between the ZPL and the PSB is about 170 meV, as highlighted by the vertical dotted line. Spectra are normalized and offset vertically for clarity. White scale bar in all images is  $10 \, \mu \text{m}$ .

experimental findings report a second type of color center in hBN that is energetically spread over a broader range between 1.5 and 2.2 eV and displays relatively narrow ZPL line width as compared to the type I emitter with values down to 0.4 meV<sup>18</sup> at cryogenic temperatures and 1.2 meV<sup>19</sup> as well as significantly reduced PSB coupling. We refer to this center in the following as the "type II" defect center in hBN. Although important for the development of spin—photon interfaces in 2D materials, the magneto-optical properties of color centers in hBN are currently unknown. In addition, the problem of blinking and spectral diffusion (SD), a common detrimental problem in narrowband quantum emitters such as quantum dots, 23 carbon nanotubes, 24-26 NV centers in diamond, 27 ZnO, 28 and recently also observed in hBN, 29 has not yet been solved or eliminated for the quantum emitters in hBN.

Here, we show that individual type II quantum emitters in hBN are spatially correlated with structural defects and can display ultranarrow ZPL line widths down to 45  $\mu$ eV if SD and blinking are effectively reduced by more than 1 order of magnitude with a surface passivation technique. We further show that the type II emitter appears spatially independent of the type I emitter and is characterized by a PSB contribution relative to the intensity of the ZPL as small as 2%. We have furthermore established the magneto-optical characterization of quantum light emitters in hBN, revealing cycling optical transitions for the type II defect with an upper bound for the g-factor of 0.2  $\pm$  0.2, in agreement with our spin-polarized DFT calculations for defect states in hBN predicting possible commensurate optical transitions in the relevant energy range.

## **RESULTS AND DISCUSSION**

With the goal to create optically active defect centers in multilayer hBN, the chemical vapor deposition (CVD)-grown material was transferred onto  $SiO_2/Si$  wafers and annealed at 850 °C in argon gas (see Methods). Figure 1a shows multilayer hBN on top of a gold marker substrate, revealing some wrinkles introduced by the transfer process as well as a clear transition to the bare  $SiO_2$  substrate. Under sub-bandgap excitation of 532 nm

laser light, a confocal photoluminescence (PL) map was recorded of the spectrally broad and nearly omnipresent color center emission signal with its zero-phonon line (ZPL) centered around 2.13 eV (Figure 1b). The optical emission appears dark, that is, strongly quenched when on top of the Au marker, as expected from the dominant nonradiative energy transfer when optical materials are in direct contact with metals. In contrast, the optical emission is significantly brighter along the wrinkles, indicating that this emission is sensitive to strain and/or local lattice symmetry distortions.

In an attempt to further enhance the emission intensity, we have investigated regions of the hBN layer where microscopic structural defects are visible. Figure 1c shows a region with a crack a few microns long that can appear as a result of the stress relaxation of the hBN layer after the high-temperature annealing. The vicinity of these cracks is decorated with several PL hot spots with one typical spectrum shown in Figure 1e. The PL spectrum for position P1 is dominated by a rather broad ZPL with a full width at half-maximum (fwhm) of about 45 meV followed by a strong PSB positioned 160 meV lower with a peak height ratio of 0.75 for the one-phonon and 0.4 for the two-phonon sideband relative to the ZPL peak intensity. The corresponding Debye-Waller (DW) factor that characterizes the strength of the electron—phonon coupling can be estimated from the ratio of the integrated ZPL intensity over the integrated total emitter intensity that includes the emission bandwidth of the PSB region. 30,31 The emitter located at P1 is characterized by a rather low DW factor of 0.29, indicating that it is affected by strong and detrimental PSB emission. This spectrum resembles the characteristic emission of the type  $\bar{I}$  defect center in hBN. Spectra recorded away from the hotspot (e.g., position B1) show a similar spectrum albeit with lower intensity and are the basis for the 2D scan shown in Figure 1b.

In striking contrast to the type I emitter, one can also find extremely sharp spectral lines that we labeled in the following as "type II" defect emission. While these sharp lines appear in Figure 1e together in the same spectrum with the broadband type I emission, we show in Figure 1f evidence (e.g., position P4) that

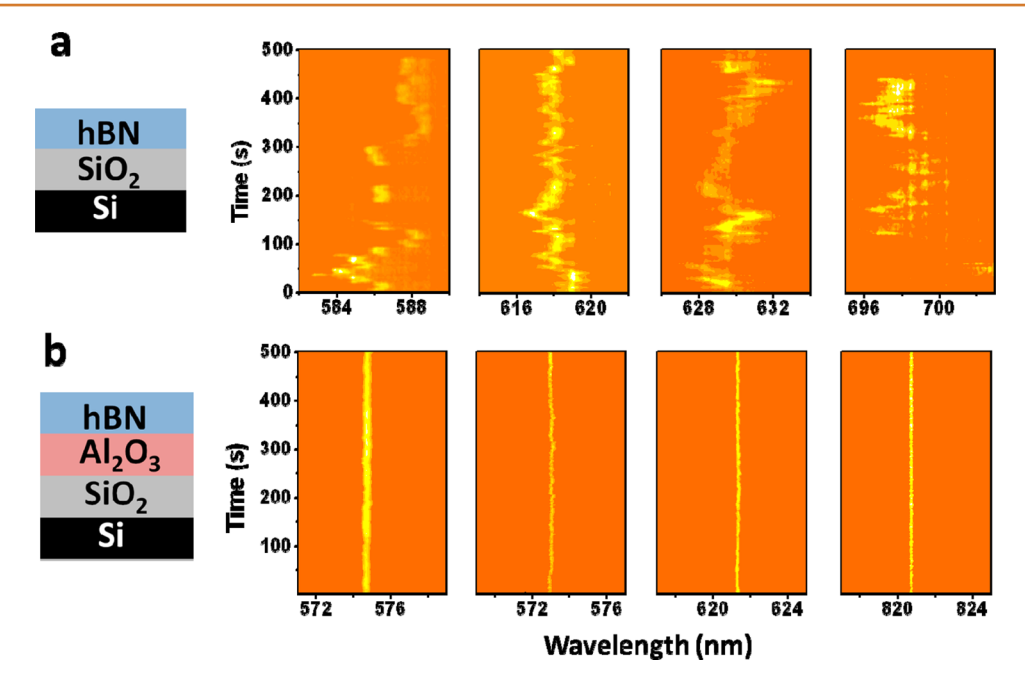


Figure 2. Spectral trajectory of type II emission in hBN. (a) Spectral trajectories taken for the type II emission from four different spatial locations for the case that hBN is located directly on an  $SiO_2$  substrate. (b) Spectral trajectories for the case that hBN is located on top of an ALD-grown  $Al_2O_3$  spacer layer with a thickness of 2 nm. All data are recorded at pump powers of 21  $\mu$ W with 1 s integration time per frame. To guide visual comparison and illustrate the significant spectral diffusion suppression, the wavelength interval of the x-axis was fixed to 8 nm in all cases.

they can also occur without an accompanying type I emission center and must therefore be considered as a separate defect center in hBN of unknown microscopic origin. As the spatially resolved images suggest, the type II emission predominantly occurs near edges and/or structural defects in the basal plane. In the following, we focus our investigation on the spectrally narrow type II emitters.

A study of the time dynamics of the optical emission from the type II defect reveals that it is not stable over time and undergoes extensive spectral diffusion. The spectra in Figure 2a show four exemplary cases of the temporal evolution of individual single spectral lines recorded from separate locations on the sample and for the case of hBN being directly transferred onto a SiO2 substrate. Over a period of 500 s, the optical emission carries out SD over a spectral range of up to 9 nm as well as blinking with very pronounced off states, where the emitter undergoes nonradiative recombination for up to 50 s before recovering into its bright state (e.g., first panel in Figure 2a). This behavior is found over the entire emission range from 580 to 700 nm. Both blinking and SD in quantum emitters are very detrimental from a technological point of view as they imply low quantum yields and make coupling to high-quality cavity modes impractical. One recent study on type I emitters explored capping hBN with poly(methyl)methacrylate (PMMA), but this did not result in significant reduction of SD and blinking.<sup>29</sup> As we have shown for the case of carbon nanotube excitons, the cause of SD and blinking can be related to mobile charges within surface-bound water onto the SiO<sub>2</sub> surface and can be effectively prevented by embedding the active quantum emitter material in a nonpolar polystyrene matrix instead of polar PMMA.<sup>24-26</sup> However, because spin-coated polymers are typically 100 nm or thicker and thus less suitable if, for example, integration with highly localized nanocavity modes is anticipated, we explored here a different route based on atomic layer deposition (ALD) of a 2 nm thin Al<sub>2</sub>O<sub>3</sub> spacer layer between SiO<sub>2</sub> and the hBN. The resulting optical emission of the type II defect emission appears now

significantly narrower (Figure 2b) and, more importantly, displays largely reduced SD and blinking over the entire measurement period and wavelength range from 570 to 820 nm. As a result, the optical emission from the type II emission is now also brighter as it no longer undergoes jumps into a nonradiative off state for extended periods of time.

To further quantify the degree of SD reduction, we have analyzed 56 type II quantum emitters and determined the wavelength range  $\Delta \lambda$  over which optical emission can be observed within the 500 s observation period. The  $\Delta\lambda$  values that characterize the SD bandwidth have been estimated by plotting all spectra in the same viewgraph (see Figure S1). The top panel in Figure 3 shows the occurrence histogram for the  $\Delta\lambda$  values for the case that hBN is directly transferred onto the SiO<sub>2</sub> substrate. In this case, the average SD bandwidth is 5 nm with a worst case of 9 nm. Pronounced SD reduction down to an average  $\Delta \lambda$  value of 1.5 nm is observed when hBN is transferred onto wafers that are overgrown with 2 nm Al<sub>2</sub>O<sub>3</sub> using ALD. For this experiment, shown in the middle panel of Figure 3, we have chosen material from the edge of the wafer, where the growth is known to be rather nonuniform due to the geometry constrains in the ALD chamber, and transferred hBN material from the same CVD growth run onto it. Significantly better results are obtained if high-quality Al<sub>2</sub>O<sub>3</sub> taken from the center of the wafer is utilized. As shown in the bottom panel of Figure 3, the average narrows down to  $\Delta \lambda = 0.4$  nm with the best case being as narrow as 0.1 nm, again with hBN from the same CVD growth run. These findings demonstrate that the uniformity of the Al<sub>2</sub>O<sub>3</sub> layer is important when this technique is employed to suppress detrimental SD in 2D materials.

With the problem of SD and blinking solved for the purpose of recording high-resolution spectra, we now turn to a detailed study of the quantum optical and magneto-optical properties of the type II emission centers in  $Al_2O_3/hBN$  samples. As a first indication that the emission from type II emitters occurs from an individual two-level system confined in 0D, we note that the

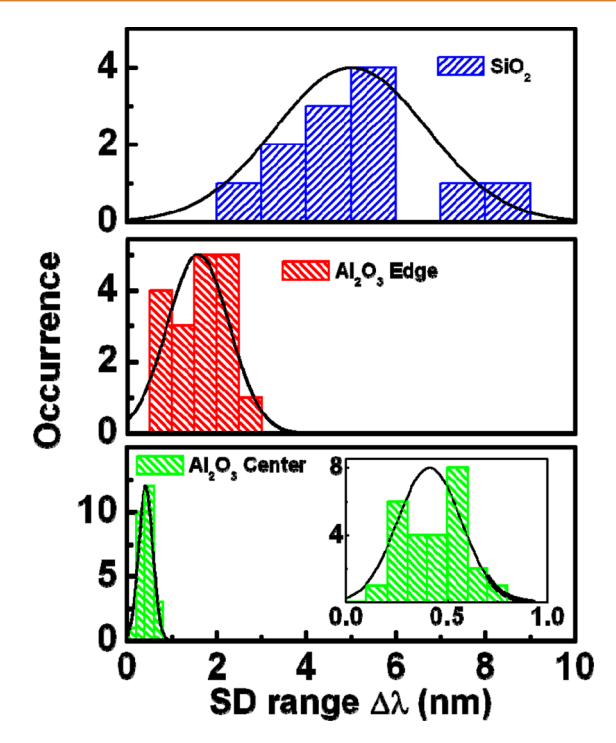


Figure 3. Statistical analysis of spectral diffusion wavelength range  $\Delta\lambda$  for 56 type II emitters. The top panel shows the  $\Delta\lambda$  occurrence histogram for hBN directly on SiO<sub>2</sub> substrate with an average value of 5 nm and a worst case of 9 nm. Middle panel: Histogram for the case that hBN is located on nonuniform Al<sub>2</sub>O<sub>3</sub> material taken from the edge of the wafer. Average:  $\Delta\lambda$  = 1.5 nm. Bottom panel: Histogram for the case that hBN is on uniform Al<sub>2</sub>O<sub>3</sub> from the center of the wafer. The inset zooms into the *x*-axis of the same data set. Average:  $\Delta\lambda$  = 0.4 nm with a best case of 0.1 nm. All data are recorded at pump powers of 21  $\mu$ W.

blinking pattern in some traces of Figure 2a switches fully off in the dark state during the quantum jumps. This is in contrast to emission from extended emitters such as 1D nanostructures, where several excitons can populate the 1D density of states and are known to never fully switch off in the dark state. 24,25 Another indication for 0D localization is the pronounced saturation behavior shown in Figure 4a, which displays integrated emission intensity as a function of excitation power for an individual type II emitter. Assuming emission occurs from an effective two-level system that gets populated through continuous wave pumping from an excited state, one can model the trend in Figure 4a using the standard rate equation analysis resulting in  $I = I_s P/(P + P_s)$ , where  $I_s$  and  $P_s$  are the PL intensity and pump power at saturation.<sup>32</sup> From this analysis, which is shown as a solid line in Figure 4a, a low saturation power of  $P_s = 170 \pm 15 \,\mu\text{W}$  is found. Such low saturation power levels are typical for 0D confined quantum emitters such as excitons in semiconductor quantum dots<sup>33</sup> and are unlikely to have their origin in many-body effects such as exciton-exciton annihilation that are typically responsible for saturation in 1D or 2D systems but set in only at orders of magnitude higher pump powers than observed here. In saturation, count rates up to  $I_s = 1.3$  kHz are found. Taking into account for the total detection efficiency of our setup (8.3%), this results in an emitter count rate of 15.6 kHz into the first lens. We note that these count rate values are quite comparable to the exciton emission from individual polymerwrapped carbon nanotubes pumped near saturation, where we find typical count rates of about 2-3 kHz when recorded in the same setup. Since the quantum yield is known for these carbon nanotubes to be about 2%, as determined from photon antibunching measurements,<sup>34</sup> one can get a rough estimate for the quantum yield of type II emitters in hBN of about 1%.

To directly prove that the emission from the type II centers originates from a solitary defect or dopant atom in the hBN material, we have recorded the second-order photon correlation function  $g^{(2)}(\tau)$  under continuous laser excitation (Figure 4a

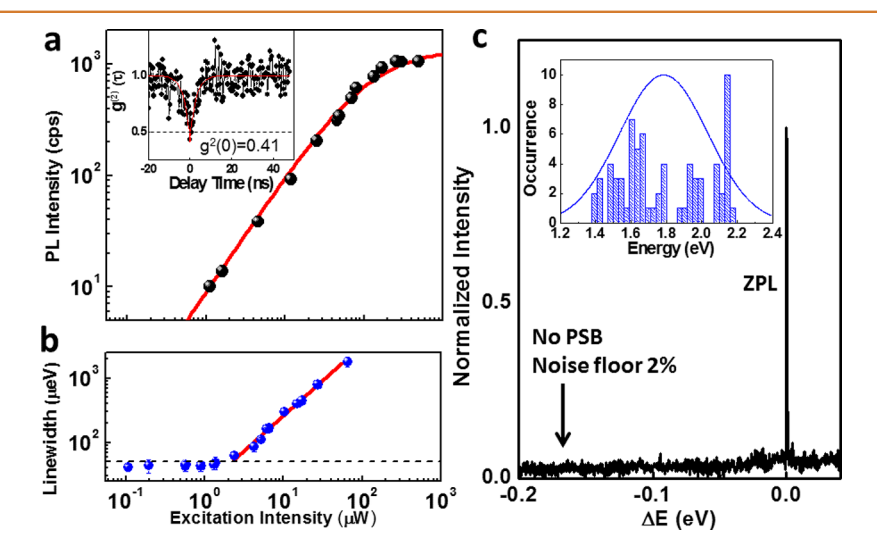


Figure 4. Photophysical properties of type II emitters in hBN. (a) PL intensity *versus* pump power (black dots); cps: counts per second. The red solid line is a fit from a rate equation analysis of a two-level system. The inset shows the second-order photon correlation function  $g^{(2)}(\tau)$  recorded under continuous wave excitation by filtering the PL signal with a 10 nm bandpass. Pronounced antibunching is visible with  $g^{(2)}(0) = 0.41$ . Dashed line illustrates the single emitter regime  $g^{(2)} = 0.5$ . (b) Lorentzian line width values extracted from a Voigt deconvolution with the system response (55  $\mu$ eV) plotted as a function of pump power. The dashed line indicates the system resolution limit, and the solid line is a guide for the eye illustrating the pump-induced emitter dephasing. (c) Normalized emission spectrum for a type II emitter showing a clean ZPL for a quantum emitter at 820 nm (1.51 eV) and no significant PSB emission above the noise floor of 2%. Inset: Histogram of the emission energy distribution for 72 type II emitters.

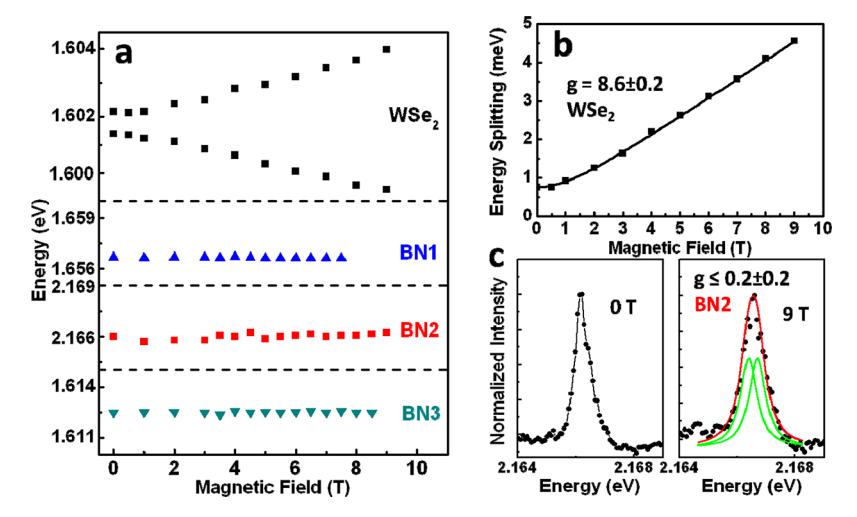


Figure 5. Magneto-PL properties of type II quantum emitters in hBN and their comparison to WSe $_2$  quantum emitters. (a) Energy position for the optical transition determined from Lorentzian line shape analysis *versus* magnetic field. BN1–BN3 represent three different sample positions showing hot spots similar to P1–P4 in Figure 1. Data for strain-induced quantum emitters in WSe $_2$  are shown for comparison. (b) Zeeman splitting energy  $\Delta E$  for a quantum emitter in WSe $_2$  as a function of magnetic field. (c) PL spectrum of BN1 taken at magnetic field of 0 T (left panel) and 9 T (right panel). Lorentzian fits reveal 430  $\mu$ eV at 0 T and 555  $\mu$ eV at 9 T. To illustrate possible Zeeman splitting as cause of broadening, two Lorentzian lines are shown (green) together with the sum spectrum (red), leading to an upper bound estimate for the g-factor of 0.2  $\pm$  0.2. All data for hBN are recorded at pump powers of 10  $\mu$ W and 3.8 K base temperature.

inset). Pronounced photon antibunching is observed with a zerodelay time dip following the relation  $g^{(2)}(\tau) = 1 - a \exp(-|\tau|/\tau_0)$ , where parameter a quantifies the background of uncorrelated photons and  $\tau_0$  is the antibunching recovery time. Best fits are found with  $\tau_0 = 2.9$  ns and a zero-delay time value of  $g^{(2)}(0) =$ 0.41 matching the experimental data point at zero-delay time and reaching into the single emitter regime. For a single-photon emitter with a background, the zero-delay time peak area is increased by  $1 - \rho^2$  with  $\rho = S/(S+B)$ , where S and B are signal and background contributions, respectively. 32,33 A closer look at the specific type II emitter line shape reveals that a broad featureless background of B = 26% that passes the 10 nm bandpass filter contributes to the signal (S = 74%) of this type II emitter spectrum (see Supporting Figure S2), leading to  $\rho = 0.76$ and an expected  $g_b^{(2)} = 0.46$  in the presence of this background. Reducing the bandpass to 5 nm yields  $g_b^{(2)}(0) = 0.36$  for this spectrum. It is thus clear that the sharp line spectrum originates from the emission of a solitary defect center plus contribution of uncorrelated background photons, rather than an accidental contribution of two independent quantum emitters for which a theoretical value of  $g^{(2)}(0) = 0.5$  would be expected in the ideal background free case.<sup>35</sup>

We also find a number of optical signatures of the type II emitter that clearly distinguishes them from the type I defect center emission in hBN. Most striking, the line width of the ZPL reaches down to a resolution limited value of only 43  $\pm$  5  $\mu$ eV under low excitation powers of about 1  $\mu$ W, as shown in Figure 4b (see Methods). Examples of the Voigt deconvolution procedure to determine the fwhm are illustrated in Figure S2. The measured ZPL line width of type II is 3 orders of magnitude narrower than the 45 meV found for type I emitters located in the same hBN sample, that is, from the same CVD growth run and in the same dielectric environment (Figure 1e). Most previous work reports rather broad ZPL line width values of type I emitters (several meV). Two recent studies find spectral characteristics similar to the type II emission in our work, albeit with resolution limited line width values of 0.4 meV<sup>18</sup> or nonresolution-limited values of 1.2 meV<sup>19</sup> that are nevertheless

about 1 order of magnitude larger than our findings. With increasing excitation power, the ZPL line width  $\Gamma$  broadens significantly following a linear dependence. In general, spontaneous emission  $(T_1 \text{ time})$  and emitter dephasing  $(T_2 \text{ time})$ time) contribute to the spectral line width. A good measure for the  $T_1$  time can be taken from the antibunching recovery time of  $\tau_0$  = 2.9 ns, which represents  $T_1$  in the limit of low excitation. At these values, the contribution from  $T_1$  to  $\Gamma$  with values below 1  $\mu$ eV is negligible, indicating that the type II emitter line width is dominated by pump-induced dephasing processes. The exact microscopic origin is unknown but likely caused by the interplay of weak laser-induced heating promoting acoustic phonon dephasing, pump-density-dependent carrier scattering effects, and pump-induced SD processes at fast time scales, similar to previous findings of quantum emitters.<sup>36</sup> One can calculate the coherence time  $T_2$  of the optical emission using the relation  $\Gamma$  =  $2\hbar/T_2$ . For the case that pump-induced dephasing is minimized (1  $\mu$ W pump power), we determine a lower limit for the  $T_2$ coherence time of 32 ps for the optical emission from type II quantum emitters.

In addition, whereas the type I emission in Figure 1e follows the well-established pattern with strong PSB contributions, indicating pronounced coupling of optical phonons with low DW factor of 0.29, the type II emission depicted in Figure 4c appears to be largely free of PSB emission. From the noise floor in the spectrum around -170 meV away from the ZPL, one can estimate an upper bound for the contribution of the first phonon replica relative to the intensity of the ZPL to be as small as 2% (noise floor). While one cannot accurately calculate the corresponding DW factor in the absence of a signal above the noise floor, as the spectral distribution of the phonon wings and their weights are unknown, it is clear that the electron-phonon coupling is very weak for type II emitters; that is, the DW factor approaches unity, as is the case for the Si vacancy center in diamond (DW = 0.88).<sup>31</sup> These findings are in strong contrast to the type I emitters in hBN (DW = 0.29) or the well-established NV centers in diamond that typically display ZPL contributions

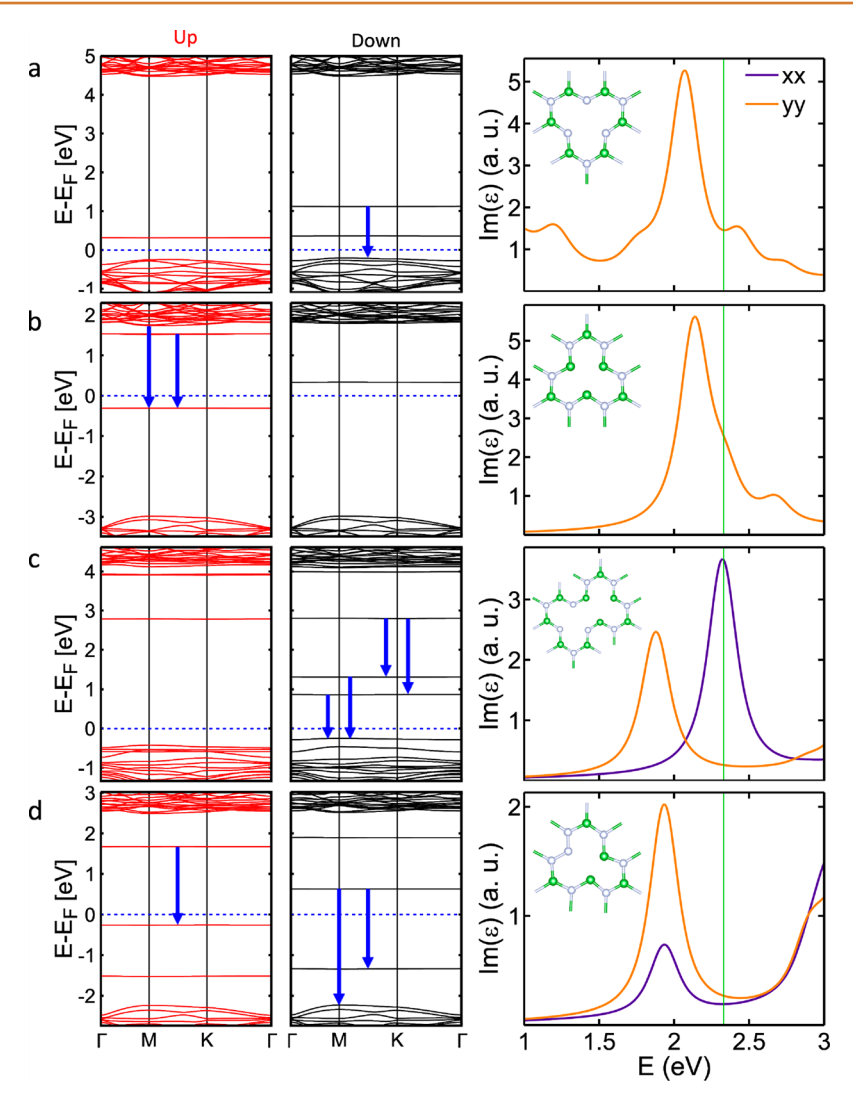


Figure 6. Spin-polarized DFT predictions of the electronic structure and optical properties of mono- and divacancies in single-layer hBN. Four defects were considered, including the (a) B vacancy  $(V_B)$ , (b) N vacancy  $(V_N)$ , (c) divacancy  $(V_{BN})$ , and (d) B vacancy with the N atom shifted over into the empty site  $(N_BV_N)$ . The spin-polarized band structures are visualized with up contributions in red (first column) and down contributions in black (second column). The blue dashed line is the Fermi level. The third column contains the imaginary part of the xx and yy components of the dielectric tensor (z direction out of plane). The green vertical line indicates the energy of the excitation laser (532 nm). Each inset features an atomic model of the relaxed defect structure. The blue arrows pointing downward illustrate possible transitions between electronic levels with like-spins that would create optical emission in the energy range matching the type II defect center emission.

to the total emission of only about 2% (i.e., a DW factor of 0.02). 30

Another remarkable characteristic of the type II emission is the rather broad energy distribution. The inset of Figure 4c shows that the 72 cases of type II emitters studied in our samples are distributed over the entire spectral region from 1.4 to 2.3 eV covering almost one octave in frequency. Some of these sharp emission lines can ride just on top of the broad ZPL of the type I emission centers, typically located around 2.2 eV. Such a broad distribution of energies is not expected from emission resulting from impurity-bound excitons with substitutional donors or acceptors, which would lead to distinct and well-defined emission energies like it is known, for example, for quantum emitters in 2D ZnSe doped with nitrogen acceptors.<sup>32</sup> The observed broad energy distribution suggests that the defect center couples to local lattice strain similar to recent findings of strain-induced localization of exciton quantum emitters in 2D transition metal dichalcogenides that can also cover hundreds of nanometer spectral range depending on local strain.<sup>37–40</sup> Recent studies on

hBN also observed emitter energy variations over a comparable range, <sup>18,19</sup> whereas one experiment that directly applies strain to hBN demonstrates at least small but reversible strain-induced energy shifts up to 6 meV. <sup>41</sup>

Finally, we explored the magneto-optical properties of the type II emitters by applying a magnetic field from 0 to 9 T in a Faraday geometry (k-vector perpendicular to the 2D plane). Interestingly, the emission spectra of type II centers remain largely unaffected with increasing magnetic field and do not split or shift energetically beyond an observed small jitter in their energy position, as shown for three cases labeled BN1–BN3 in Figure 5a. This is in stark contrast to the behavior of other color centers or 0D localized exciton emission in semiconductors. For comparison, we show in Figure 5a the magneto-PL behavior of a strain-localized exciton emission centers from monolayer WSe<sub>2</sub> that is characterized by a pronounced doublet with a zero-field splitting energy of 760  $\mu$ eV that follows a Zeeman splitting pattern with increasing magnetic field. The resulting energy splitting  $\Delta E$  is plotted in Figure 5b and follows the well-known

relation  $\Delta E = \sqrt{{\Delta_0}^2 + (\mu_B g B)^2}$ , where  $\Delta_0$  is the zero-field splitting energy,  $\mu_B$  is the Bohr magneton, and B is the magnetic field strength, resulting in a gyromagnetic ratio of  $g = 8.6 \pm 0.2$ . While no apparent energy shift or splitting is observed for the type II emitter in hBN, one can notice a slight broadening of the ZPL from initially 430  $\mu eV$  at 0 T to 555  $\mu eV$  at 9 T, as determined from fits to single Lorentzian lines (Figure Sc). Assuming the asymmetry is caused by an underlying spectrally unresolved Zeeman splitting, one can fit two Lorentzian subcomponents (green solid lines) to model the line shape resulting in a peak splitting of 125  $\mu eV$  that corresponds to an upper bound for the BN2 g-factor of  $g \le 0.2 \pm 0.2$ .

This apparent nonmagnetic behavior of type II emitters in hBN with an effective Landé factor well below the value for pure orbit (1) or pure spin (2) is likely to have its origin in cycling optical transition between two states with nearly commensurate Landé factors, that is, same spin states, similar to the chromiumbased color centers<sup>21</sup> or the silicon vacancy centers in diamond.<sup>22</sup> To further investigate the situation for hBN, we have investigated the electronic properties of defects in single-layer hBN using collinear spin-polarized DFT calculations. Details of the calculations are deferred to the theoretical Methods section. Four defects were considered, including the B vacancy (VB, Figure 6a), N vacancy (V<sub>N</sub>, Figure 6b), divacancy (V<sub>BN</sub>, Figure 6c), and B vacancy with the N atom shifted over into the empty site (N<sub>B</sub>V<sub>N</sub>, Figure 6d). The N vacancy with the B atom shifted over into the empty site is not stable; that is, the system relaxes back to the standard N vacancy configuration. For each defect, the spin-polarized electronic band structure is presented (red = up and black = down) using the PBE exchange correlation energy functional. The nearly flat bands with large effective mass correspond to the energy levels localized at defects. To gain insight into the absorption properties, the in-plane diagonal components of the dielectric tensor were computed. The strongest absorption occurs around 5.5 eV in each case, corresponding to the absorption across the hBN band gap (not shown). Each of the structures has a sizable absorption resonance at the pump laser wavelength (532 nm, 2.3 eV), as highlighted by the green line in the third column of Figure 6.

Assuming the laser pumps electrons into defect levels and leaves holes in the valence band, several possibilities exist where only like-spin transitions are involved in the optical recombination, as illustrated by the blue arrows pointing downward. The corresponding transition energies of about 1.3-2.5 eV match the type II emitter energy range (see Figure 4c, inset). Interestingly, V<sub>B</sub>, V<sub>N</sub>, and V<sub>BN</sub> have pairs of energy levels for one spin orientation with energy differences in the experimentally observed range and no such pairs for the opposite spin. Because the energy levels with like-spins shift in the same direction and do not split in a magnetic field, it is apparent that the corresponding optical transitions between them do not show a magnetic behavior, in agreement with the experimental observations. In addition, several possible transitions can occur between defect levels alone that do not involve the band edges and can therefore be decoupled from the bulk phonons; that is, small electron phonon coupling is expected, in agreement with the absence of phonon sidebands for the type II emitter. We note that whereas an exact identification of the microscopic configurations responsible for either type I or type II emission is rather difficult, the matching of the energy range and presence of several likespin transitions in the considered native hBN defects, particularly the divacancy, is already striking.

#### **CONCLUSIONS**

In summary, we have demonstrated that individual type II quantum emitters in hBN are spatially correlated with structural defects and can display an ultranarrow zero-phonon line width down to 45  $\mu eV$  corresponding to a dephasing time of 32 ps. These results have been achieved by utilizing a passivation technique based on high-quality atomic layer epitaxy grown Al<sub>2</sub>O<sub>3</sub> that effectively reduces detrimental spectral diffusion from the substrate by more than 1 order of magnitude. The best line widths are 3 orders of magnitude narrower compared to type I defect centers in the same sample and 1 order of magnitude narrower when compared to previous reports on type II emitters. We have also presented evidence that undesired emission into optical phonon sidebands is largely absent for this type of emitter contributing not more than 2% relative to the peak intensity of the zero-phonon line, that is, DW factors approaching unity. In addition, we established the magneto-optical characterization of quantum light emitters in hBN and found that the type II defect center is nonmagnetic when probed in Faraday geometry, implying cycling optical transitions and an upper bound for the gfactor of  $0.2 \pm 0.2$ . These findings are in excellent agreement with our spin-polarized DFT calculations of native defect states in hBN which show that transitions in the experimental energy range occur in only one spin configuration for the V<sub>B</sub>, V<sub>N</sub>, and  $V_{BN}$  defects. The  $V_{BN}$  defect also has a significant optical absorption at the green pump laser wavelength and could be responsible for the type II emission. Future work should also address defect configurations with larger extension beyond the divacancy such as hBN edges in general (armchair and zigzag type) that might also allow for direct patterning. 42 Our results are of interest toward the realization of narrowband quantum light emitters emitting indistinguishable photons, particularly when coupled to nanocavity modes for Purcell-enhanced light extraction that can overcome the current limitations of low quantum efficiency of this type II emitter displaying rather moderate photon emission rates of 15.6 kHz into the first lens. They are also a first critical step toward the development of efficient spin-photon interfaces within 2D materials for future chip-scale quantum networks.

### **METHODS**

Sample Preparation. Multilayer hBN was grown by chemical vapor deposition on copper foil from borazine precursor (Graphene Supermarket). The multilayer material has a typical layer thickness of 13 nm. To transfer the as-grown material, PMMA in chlorobenzene (950 C4) was spin-coated (200 rpm) onto the hBN film and baked at 60 °C for 5 min. Samples were placed in copper etchant (Transene) at 100 °C for 12 h to dissolve the copper foil. The resultant multilayer hBN/ PMMA films were transferred onto either regular 90 nm SiO<sub>2</sub>/Si substrates or Al<sub>2</sub>O<sub>3</sub>/SiO<sub>2</sub>/Si substrates, where a 2 nm thick layer of Al<sub>2</sub>O<sub>3</sub> was deposited by atomic layer deposition to effectively remove spectral diffusion. To remove the PMMA stabilization layer, samples were first rinsed with warm acetone and then annealed in an ultrahigh vacuum chamber on top of a button heater (Heatwave Laboratories) for 12 h at 350 °C to fully remove any residual polymer contamination. To activate the color/defect centers, samples were annealed at 850 °C for 30 min in the same chamber under 1 Torr of argon to prevent oxidation.

**Optical Measurements.** Microphotoluminescence ( $\mu$ -PL) and magnetic field measurements were taken inside a closed-cycle He cryostat with a 3.8 K base temperature and a superconducting magnet that can apply a field up to 9 T (attodry1100). Samples were excited with a solid-state pumped laser diode operating at 532 nm in continuous wave mode. A 532 nm interference filter was used in front of the green laser to suppress the 808 nm pump diode laser light. An Abbe limited laser spot size of about 500 nm was achieved using a cryogenic

microscope objective with numerical aperture of 0.82. The relative position between sample and laser spot was adjusted with cryogenic piezoelectric *xyz*-stepper (attocube), whereas 2D PL images were created with a piezoscanner module (attocube). The spectral emission was recorded with a multimode fiber and sent to a single-photon counting avalanche silicon photodiode (PerkinElmer APD). PL spectra were recorded with a 0.75 m focal length spectrometer connected to a liquid-nitrogen-cooled CCD camera. Laser stray light was rejected using two long-pass 550 nm filters.

**Photon Correlation Measurements.** The second-order photon correlation function  $g^2(\tau)$  was recorded *via* time-correlated single-photon counting by sending the PL emission through narrow bandpass filters and a Hanbury-Brown and Twiss setup consisting of a fiber-coupled 50/50 beam splitter connected to two silicon APDs. A linear polarizer was used in the collection path for photon antibunching measurements. Coincidence counts were time stamped and analyzed with a high-resolution timing module (SensL).

Theoretical Methods. Plane-wave DFT calculations were carried out within the Vienna Ab Initio Simulation Package (VASP). Exchange and correlation were included via the PBE functional.44 Projector-augmented wave (PAW) pseudopotentials were implemented with an energy cutoff of 450 eV. 45 A tolerance of 10<sup>-5</sup> eV was set for the electronic convergence, and Gaussian smearing of 0.05 eV was employed. For the primitive cell of single-layer hBN (z direction perpendicular to layer), a Monkhorst–Pack k-point sampling of  $7 \times 7 \times 7 \times 7 \times 10^{-5}$ 1 was used. 46 The cell and atoms were relaxed to a force cutoff of 0.01 eV/Å, which resulted in an optimized in-plane lattice constant of 2.51 Å. This force cutoff is implied in subsequent relaxations. A large vacuum layer of 20 Å was set to prevent spurious interactions between periodic replicas. Mono- and divacancies in hBN were modeled with a 7 × 7 supercell and a k-point sampling of  $1 \times 1 \times 1$ . The atoms were first relaxed without and then subsequently with collinear spin-polarization (up and down spins along z direction). In the calculation of the spinpolarized electronic band structures, 450 bands were used and 48 unique k-points were chosen along the high-symmetry directions in total. The dielectric function was calculated within the independent particle approximation and neglecting local field effects using 504 bands. 47 We note that whereas PBE appears to accurately predict the experimentally observed band gap of ~6.0 eV, this result should not be interpreted as quantitative accuracy of the PBE functional. A systematic cancelation of errors occurs in neglecting excitonic effects, screening and reduced quantum confinement in multilayers, substrate renormalization of the band gap, and the general behavior of PBE to underestimate the band gap. Despite this, the accurate prediction of the band gap is expected to provide a reasonable picture of the spacing of the in-gap defect levels. The properties of simple defects in single-layer hBN have been studied previously. <sup>13,48–50</sup> However, in these previous studies, the electronic band structures and optical absorption properties were not both calculated for all four defects using identical methods and techniques. This makes it difficult to operate a reliable comparison between calculated properties and the experimental data because such a comparison requires consistency in the method and parameter settings.

### **ASSOCIATED CONTENT**

#### S Supporting Information

The Supporting Information is available free of charge on the ACS Publications website at DOI: 10.1021/acsnano.7b00638.

Method for determining spectral diffusion wavelength range in Figure S1, analysis of photon correlation measurements in the presence of uncorrelated background in Figure S2, detailed line width analysis *via* Voigt deconvolution procedure in Figure S3 (PDF)

#### **AUTHOR INFORMATION**

#### **Corresponding Author**

\*E-mail: strauf@stevens.edu.

#### ORCID ®

Stefan Strauf: 0000-0002-9887-7059

#### Notes

The authors declare no competing financial interest.

#### **ACKNOWLEDGMENTS**

We would like to thank Milan Begliarbekov for supporting the ALD at the City University of New York Advanced Science Research Center (ASRC) nanofabrication facility. S.S. acknowledges financial support by the National Science Foundation (NSF) under awards DMR-1506711, ECCS-MRI-1531237, and EFRI-ACQUIRE-1641094. A.C. and V.M. acknowledge financial support by NSF Grant EFRI 2-DARE (EFRI-1542707).

#### **REFERENCES**

- (1) Cassabois, G.; Valvin, P.; Gil, B. Hexagonal Boron Nitride is an Indirect Bandgap Semiconductor. *Nat. Photonics* **2016**, *10*, 262–266.
- (2) Wang, X.; Xia, F. Van der Waals Heterostructures: Stacked 2D Materials Shed Light. *Nat. Mater.* **2015**, *14*, 264–265.
- (3) Dean, C. R.; Young, A. F.; Meric, I.; Lee, C.; Wang, L.; Sorgenfrei, S.; Watanabe, K.; Taniguchi, T.; Kim, P.; Shepard, K. L.; Hone, J. Boron Nitride Substrates for High-quality Graphene Electronics. *Nat. Nanotechnol.* **2010**, *5*, 722–726.
- (4) Lee, G. H.; Yu, Y. J.; Cui, X.; Petrone, N.; Lee, C. H.; Choi, M. S.; Lee, D. Y.; Lee, C.; Yoo, W. J.; Watanabe, K.; Taniguchi, T.; Nuckolls, C.; Kim, P.; Hone, J. Flexible and Transparent MoS<sub>2</sub> Field-Effect Transistors on Hexagonal Boron Nitride-Graphene Heterostructures. *ACS Nano* **2013**, *7*, 7931–7936.
- (5) Radisavljevic, B.; Radenovic, A.; Brivio, J.; Giacometti, V.; Kis, A. Single-Layer MoS<sub>2</sub> Transistors. *Nat. Nanotechnol.* **2011**, *6*, 147–150.
- (6) Lee, K. H.; Shin, H. J.; Lee, J.; Lee, I.; Kim, G. H.; Choi, J. Y.; Kim, S. W. Large-Scale Synthesis of High-Quality Hexagonal Boron Nitride Nanosheets for Large-Area Graphene Electronics. *Nano Lett.* **2012**, *12*, 714–718.
- (7) Batalov, A.; Zierl, C.; Gaebel, T.; Neumann, P.; Chan, I. Y.; Balasubramanian, G.; Hemmer, P. R.; Jelezko, F.; Wrachtrup, J. Temporal Coherence of Photons Emitted by Single Nitrogen-Vacancy Defect Centers in Diamond Using Optical Rabi-Oscillations. *Phys. Rev. Lett.* 2008, 100, 077401.
- (8) Babinec, T. M.; Hausmann, B. J. M.; Khan, M.; Zhang, Y.; Maze, J. R.; Hemmer, P. R.; Loncar, M. A Diamond Nanowire Single-Photon Source. *Nat. Nanotechnol.* **2010**, *5*, 195–199.
- (9) Castelletto, S.; Johnson, B. C.; Ivády, V.; Stavrias, N.; Umeda, T.; Gali, A.; Ohshima, T. A Silicon Carbide Room-Temperature Single-Photon Source. *Nat. Mater.* **2013**, *13*, 151–156.
- (10) Lienhard, B.; Schröder, T.; Mouradian, S.; Dolde, F.; Tran, T. T.; Aharonovich, I.; Englund, D. Bright and Photostable Single-Photon Emitter in Silicon Carbide. *Optica* **2016**, *3*, 768.
- (11) Aharonovich, I.; Englund, D.; Toth, M. Solid-State Single-Photon Emitters. *Nat. Photonics* **2016**, *10*, 631–641.
- (12) Gao, W. B.; Fallahi, P.; Togan, E.; Miguel-Sanchez, J.; Imamoglu, A. Observation of Entanglement Between a Quantum Dot Spin and a Single Photon. *Nature* **2012**, *491*, 426–430.
- (13) Tran, T. T.; Bray, K.; Ford, M. J.; Toth, M.; Aharonovich, I. Quantum Emission from Hexagonal Boron Nitride Monolayers. *Nat. Nanotechnol.* **2015**, *11*, 37–41.
- (14) Bourrellier, R.; Meuret, S.; Tararan, A.; Stéphan, O.; Kociak, M.; Tizei, L. H. G.; Zobelli, A. Bright UV Single Photon Emission at Point Defects in h-BN. *Nano Lett.* **2016**, *16*, 4317–4321.
- (15) Chejanovsky, N.; Rezai, M.; Paolucci, F.; Kim, Y.; Rendler, T.; Rouabeh, W.; Fávaro de Oliveira, F.; Herlinger, P.; Denisenko, A.; Yang, S.; Gerhardt, I.; Finkler, A.; Smet, J. H.; Wrachtrup, J. Structural Attributes and Photodynamics of Visible Spectrum Quantum Emitters in Hexagonal Boron Nitride. *Nano Lett.* **2016**, *16*, 7037–7045.
- (16) Tran, T. T.; Zachreson, C.; Berhane, A. M.; Bray, K.; Sandstrom, R. G.; Li, L. H.; Taniguchi, T.; Watanabe, K.; Aharonovich, I.; Toth, M.

Quantum Emission from Defects in Single-Crystalline Hexagonal Boron Nitride. *Phys. Rev. Appl.* **2016**, *5*, 034005.

- (17) Martinez, L. J.; Pelini, T.; Waselowski, V.; Maze, J. R.; Gil, B.; Cassabois, G.; Jacques, V. Efficient Single Photon Emission From a High-Purity Hexagonal Boron Nitride Crystal. *Phys. Rev. B: Condens. Matter Mater. Phys.* **2016**, *94*, 121405.
- (18) Jungwirth, N. R.; Calderon, B.; Ji, Y.; Spencer, M. G.; Flatté, M. E.; Fuchs, G. D. Temperature Dependence of Wavelength Selectable Zero-Phonon Emission from Single Defects in Hexagonal Boron Nitride. *Nano Lett.* **2016**, *16*, 6052–6057.
- (19) Tran, T. T.; Elbadawi, C.; Totonjian, D.; Lobo, C. J.; Grosso, G.; Moon, H.; Englund, D. R.; Ford, M. J.; Aharonovich, I.; Toth, M. Robust Multicolor Single Photon Emission from Point Defects in Hexagonal Boron Nitride. *ACS Nano* **2016**, *10*, 7331–7338.
- (20) Faraon, A.; Barclay, P. E.; Santori, C.; Fu, K-M. C.; Beausoleil, R. G. Resonant Enhancement of the Zero-Phonon Emission from a Colour Centre in a Diamond Cavity. *Nat. Photonics* **2011**, *5*, 301–305.
- (21) Müller, T.; Aharonovich, I.; Lombez, L.; Alaverdyan, Y.; Vamivakas, A. N.; Castelletto, S.; Jelezko, F.; Wrachtrup, J.; Prawer, S.; Atatüre, M. Wide-Range Electrical Tunability of Single-Photon Emission from Chromium-Based Colour Centres in Diamond. *New J. Phys.* **2011**, *13*, 075001.
- (22) Pingault, B.; Becker, J. N.; Schulte, C. H. H.; Arend, C.; Hepp, C.; Godde, T.; Tartakovskii, A. I.; Markham, M.; Becher, C.; Atatüre, M. All-Optical Formation of Coherent Dark States of Silicon-Vacancy Spins in Diamond. *Phys. Rev. Lett.* **2014**, *113*, 263601.
- (23) Neuhauser, R. G.; Shimizu, K. T.; Woo, W. K.; Empedocles, S. A.; Bawendi, M. G. Correlation between Fluorescence Intermittency and Spectral Diffusion in Single Semiconductor Quantum Dots. *Phys. Rev. Lett.* **2000**, *85*, 3301–3304.
- (24) Ai, N.; Walden-Newman, W.; Song, Q.; Kalliakos, S.; Strauf, S. Suppression of Blinking and Enhanced Exciton Emission from Individual Carbon Nanotubes. *ACS Nano* **2011**, *5*, 2664–2670.
- (25) Walden-Newman, W.; Sarpkaya, I.; Strauf, S. Quantum Light Signatures and Nanosecond Spectral Diffusion from Cavity-Embedded Carbon Nanotubes. *Nano Lett.* **2012**, *12*, 1934–1941.
- (26) Sarpkaya, I.; Ahmadi, E. D.; Shepard, G. D.; Mistry, K. S.; Blackburn, J. L.; Strauf, S. Strong Acoustic Phonon Localization in Copolymer-Wrapped Carbon Nanotubes. *ACS Nano* **2015**, *9*, 6383–6303
- (27) Wolters, J.; Sadzak, N.; Schell, A. W.; Schröder, T.; Benson, O. Measurement of the Ultrafast Spectral Diffusion of the Optical Transition of Nitrogen Vacancy Centers in Nano-Size Diamond Using Correlation Interferometry. *Phys. Rev. Lett.* **2013**, *110*, 027401.
- (28) Neitzke, O.; Morfa, A.; Wolters, J.; Schell, A. W.; Kewes, G.; Benson, O. Investigation of Line Width Narrowing and Spectral Jumps of Single Stable Defect Centers in ZnO at Cryogenic Temperature. *Nano Lett.* **2015**, *15*, 3024–3029.
- (29) Shotan, Z.; Jayakumar, H.; Considine, C. R.; Mackoit, M.; Fedder, H.; Wrachtrup, J.; Alkauskas, A.; Doherty, M. W.; Menon, V. M.; Meriles, C. A. Photoinduced Modification of Single-Photon Emitters in Hexagonal Boron Nitride. ACS Photonics 2016, 3, 2490—2496.
- (30) Alkauskas, A.; Buckley, B. B.; Awschalom, D. D.; Van de Walle, C. G. First-Principles Theory of the Luminescence Lineshape for the Triplet Transition in Diamond NV Centres. *New J. Phys.* **2014**, *16*, 073026.
- (31) Neu, E.; Steinmetz, D.; Riedrich-Möller, J.; Gsell, S.; Fischer, M.; Schreck, M.; Becher, C. Single Photon Emission from Silicon-Vacancy Colour Centres in Chemical Vapour Deposition Nano-Diamonds on Iridium. *New J. Phys.* **2011**, *13*, 025012.
- (32) Strauf, S.; Michler, P.; Klude, M.; Hommel, D.; Bacher, G.; Forchel, A. Quantum Optical Studies on Individual Acceptor Bound Excitons in a Semiconductor. *Phys. Rev. Lett.* **2002**, *89*, 177403.
- (33) Strauf, S.; Stoltz, N. G.; Rakher, M. T.; Coldren, L. A.; Petroff, P. M.; Bouwmeester, D. High-frequency Single-Photon Source with Polarization Control. *Nat. Photonics* **2007**, *1*, 704–708.
- (34) Jeantet, A.; Chassagneux, Y.; Raynaud, C.; Roussignol, Ph.; Lauret, J. S.; Besga, B.; Estève, J.; Reichel, J.; Voisin, C. Widely Tunable

I

- Single-Photon Source from a Carbon Nanotube in the Purcell Regime. *Phys. Rev. Lett.* **2016**, *116*, 247402.
- (35) Gerardot, B. D.; Strauf, S.; de Dood, M. J. A.; Bychkov, A. M.; Badolato, A.; Hennessy, K.; Hu, E. L.; Bouwmeester, D.; Petroff, P. M. Photon Statistics from Coupled Quantum Dots. *Phys. Rev. Lett.* **2005**, 95, 137403.
- (36) Sarpkaya, I.; Zhang, Z.; Walden-Newman, W.; Wang, X.; Hone, J.; Wong, C. W.; Strauf, S. Prolonged Spontaneous Emission and Dephasing of Localized Excitons in Air-Bridged Carbon Nanotubes. *Nat. Commun.* **2013**, *4*, 2152.
- (37) Kumar, S.; Kaczmarczyk, A.; Gerardot, B. D. Strain-Induced Spatial and Spectral Isolation of Quantum Emitters in Mono- and Bilayer WSe<sub>2</sub>. *Nano Lett.* **2015**, *15*, 7567–7573.
- (38) Branny, A.; Kumar, S.; Proux, R.; Gerardot, B. D. Deterministic Strain-Induced Arrays of Quantum Emitters in a Two-Dimensional Semiconductor. *arXiv*:1610.01406 **2016**.
- (39) Shepard, G. D.; Ajayi, O.; Li, X.; Zhu, X. Y.; Hone, J.; Strauf, S. Nanobubble Induced Formation of Quantum Emitters in Monolayer Semiconductors. 2D Mater. **2017**, *4*, 021019.
- (40) Palacios-Berraquero, C.; Kara, D. M.; Montblanch, A. R. P.; Barbone, M.; Latawiec, P.; Yoon, D.; Ott, A. K.; Loncar, M.; Ferrari, A. C.; Atature, M. Large-Scale Quantum-Emitter Arrays in Atomically Thin Semiconductors. *arXiv:1609.04244* **2016**.
- (41) Grosso, G.; Moon, H.; Lienhard, B.; Ali, S.; Efetov, D. K.; Furchi, M. M.; Jarillo-Herrero, P.; Ford, M. J.; Aharonovich, I.; Englund, D. Tunable and High Purity Room-Temperature Single Photon Emission from Atomic Defects in Hexagonal Boron Nitride. *arXiv:1611.03515* 2016.
- (42) Begliarbekov, M.; Sasaki, K.-I.; Sul, O.; Yang, E. H.; Strauf, S. Optical Control of Edge Chirality in Graphene. *Nano Lett.* **2011**, *11*, 4874–4878.
- (43) Kresse, G.; Furthmüller, J. Efficient Iterative Schemes for AB Initio Total-Energy Calculations Using a Plane-Wave Basis. *Phys. Rev. B: Condens. Matter Mater. Phys.* **1996**, *54*, 11169.
- (44) Perdew, J.; Burke, K.; Ernzerhof, M. Generalized Gradient Approximation Made Simple. *Phys. Rev. Lett.* **1996**, *77*, 3865.
- (45) Blöchl, P. Projector Augmented-Wave Method. Phys. Rev. B: Condens. Matter Mater. Phys. 1994, 50, 17953.
- (46) Monkhorst, H.; Pack, J. Special Points for Brillouin-Zone Integrations. *Phys. Rev. B* **1976**, *13*, 5188.
- (47) Gajdoš, M.; Hummer, K.; Kresse, G.; Furthmüller, J.; Bechstedt, F. Linear Optical Properties in the Projector-Augmented Wave Methodology. *Phys. Rev. B: Condens. Matter Mater. Phys.* **2006**, 73, 045112.
- (48) Si, M. S.; Xue, D. S. Magnetic Properties of Vacancies in a Graphitic Boron Nitride Sheet by First-Principles Pseudopotential Calculations. *Phys. Rev. B: Condens. Matter Mater. Phys.* **200**7, 75, 102400
- (49) Attaccalite, C.; Bockstedte, M.; Marini, A.; Rubio, A.; Wirtz, L. Coupling of Excitons and Defect States in Boron-Nitride Nanostructures. *Phys. Rev. B: Condens. Matter Mater. Phys.* **2011**, *83*, 144115.
- (50) Huang, B.; Lee, H. Defect and Impurity Properties of Hexagonal Boron Nitride: A First-Principles Calculation. *Phys. Rev. B: Condens. Matter Mater. Phys.* **2012**, *86*, 245406.